University of Bath

Alternative formats
If you require this document in an alternative format, please contact:
openaccess@bath.ac.uk

Fe-, N-embedded Hierarchically Porous Carbon Architectures Derived from FeTe-trapped Zeolitic Imidazolate Frameworks as Efficient Oxygen Reduction Electrocatalysts

Minlin Mao[†§], Jiang Deng[†§], Tingting Yan[†], Junjie Shen[‡], Jianping Zhang[†], Liyi Shi[†] and Dengsong Zhang[†*]

[†] *State Key Laboratory of Advanced Special Steel, School of Materials Science and Engineering, Research Center of Nano Science and Technology, Department of Chemistry, College of Sciences, Shanghai University, No.99 Shangda Road, Shanghai, 200444, China.*

[‡] *Department of Chemical Engineering, University of Bath, Bath BA2 7AY, UK.*

[*] *E-mail: dszhang@shu.edu.cn; Tel: +86 21 66137152.*

[§] *These authors contributed equally to this work.*

ABSTRACT: During the design and construction of efficient iron-nitrogen-carbon (Fe-N-C) electrocatalyst, it was difficult to avoid the formation of iron oxides along with the hierarchical carbon frameworks containing dispersed FeN_x sites. As a result, a slow oxygen reduction reaction (ORR) occurred, making it difficult to improve the electrocatalytic property. Herein, we have successfully synthesized the Fe, N-doped hierarchically porous carbon architectures from FeTe-trapped ZIF-8 coated with polydopamine by heat treatment. During the pyrolysis process, the evaporation of tellurium could inhibit the formation of iron oxides, promote the formation of more FeN_x active species, and facilitate the formation of mesoporous structure to accelerate mass transfer and increase the approachability of active species. The resulting Fe, N-doped porous carbon architectures possessed excellent ORR catalytic performance, and the half-wave potential was 10 mV more than that of the precious Pt/C catalysts. Besides, the obtained catalysts present a superb methanol-tolerance and long-

term durability compared to precious Pt/C catalysts in alkaline media. This work opens up new avenues for the construction of the uniformly dispersed FeN$_x$ sites catalysts for ORR.

KEYWORDS: *Electrocatalysts; Porous Carbon; Oxygen reduction reaction*

■ INTRODUCTION

As the alternative clean energy technologies, fuel cells and metal-air batteries have attracted significant attention [1-2]. Oxygen reduction reaction (ORR) in the cathode undergoes a sluggish process which determines the property of fuel cells [3-8]. The platinum (Pt) catalysts are usually used as cathode materials for ORR, but its high cost, poor methanol tolerance and durability restrict the development and wide use of the fuel cell technology [9-14]. Therefore, the exploration of non-platinum catalysts with both superb activity and satisfying stability has become the most important research topic [15-21].

Recently, inspired by the ferriporphyrin in hemoglobinase, the iron-nitrogen-carbon (Fe-N-C) catalysts were developed and showed great potential as an alternative of Pt [22-27]. The concept of using Fe-N-C as the ORR catalyst was firstly developed by Jahan et al through simple loading of ferriporphyrin by graphene [28]. However, the high price of ferriporphyrin and nonefficient electron transfer hinder their wide use. Subsequently, researchers found that the Fe-N-C could be embedded in the carbon matrix which also showed promising performance toward ORR [29-32]. The primary Fe-N-C catalysts were prepared by pyrolyzing metal salts, nitrogen and carbon precursors at high temperature [33-38]. However, the unstable metallic compounds were easily migrated and aggregated in graphitic carbon shells during the uncontrolled heat treatment, resulting in lower utilization of metal species, decrement of FeN$_x$ active species, and thereby poor catalytic activity [39-42]. Therefore, it still remains a challenge to rationally design and construct high-efficiency Fe-N-C catalyst.

The remarkable Fe-N-C catalyst should have a good reaction site for oxygen-oxygen double bond

cleavage, appropriate geometric spatial structure for electrolyte transmission and O_2 diffusion, and high density of active species to maintain good performance for a long time[43-49]. The zeolitic imidazolate frameworks (ZIFs) which contained adjustable ligand structures were regarded as favorable precursors for the fabrication of Fe-N-C catalyst. Currently, some researchers [50-54] used the metal iron salt to embed the cavities of ZIF-8 to obtain the Fe-ZIF and after carbonization the resulted Fe, N-doped porous carbon had the interconnected framework structure and ultrahigh specific surface area, which exhibited excellent catalytic activity. Unfortunately, the Fe-ZIF was prone to form superabundant iron oxides particles due to the Kirkendall effect during carbonization, thus limiting its catalyticactivity [55-57]. Therefore, it has been a major ongoing research effort to establish the synergistic correlation to manifest the structure-activity relationship for ORR.

Herein, we originally developed the iron tellurium (FeTe) trapped ZIF-8 coated with polydopamine as the precursor for preparation of Fe-, N-embedded hierarchically porous carbon architectures. Te would suppress the removal of Fe by forming Te-Fe bond and inhibit the formation of iron oxides during the pyrolysis process. When the temperature exceeded the evaporation point of Te, the dispersed iron bound with N increased the density of FeN_x active site. Meanwhile, the mesoporous structure derived from evaporation of Te was able to facilitate mass transfer and enhance the approachability of the active site. Consequently, the Fe, N-doped porous carbon architectures possessed excellent ORR catalytic performance (half-wave potential was 10 mV more than the precious Pt/C catalyst) and superb the methanol-tolerant and long-term durability compared to precious Pt/C catalyst in alkaline media.
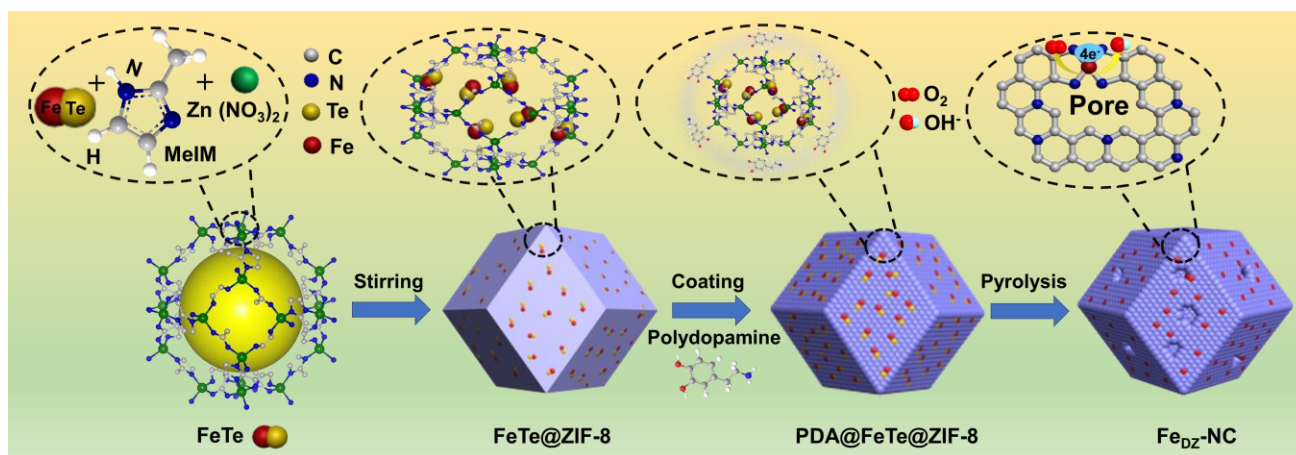
Fig 1. Schematic illustration for the synthetic procedure of Fe_{DZ}-NC catalysts.

■ EXPERIMENTAL SECTION

Materials Preparation. $Zn(NO_3)_2 \cdot 6H_2O$ (AR, 99%), $FeCl_3 \cdot 6H_2O$ (AR, 99%), 2-methyl imidazole (2-MeIM) (AR, 99%), Na_2TeO_3 (AR, 99%), CH_3OH (AR, 99.5%), ethanol (CH_3CH_2OH) (AR, 99.5%) and $N_2H_4 \cdot H_2O$ (AR, 98%) were purchased from Sinopharm Chemical Reagent Co. Ltd. Dopamine hydrochloride (98%) and trimethylolamine were supplied by Aladdin Chemistry Co. (Shanghai, China). Nafion solution and polyvinyl pyrrolidone were provided by Sigma-Aldrich.

Preparation of FeTe. $FeCl_3 \cdot 6H_2O$ (75 mM), Na_2TeO_3 (75 mM) and 2 g Polyvinyl Pyrrolidone (PVP) were dissolved into hydrazine hydrate ($N_2H_4 \cdot H_2O$, 4.5 M) and distilled water to form 40 mL homogeneous transparent solution by ultrasonic. The solutions were poured into a 100 ml hydrothermal reactor. The reactor was sealed, heated 24 h at 140^oC. The precipitates were washed several times with deionized water and CH_3CH_2OH. Finally, the materials were dried 12 h in a vacuum at 60^oC [58].

Preparation of Fe_Z-NC electrocatalysts. 100 mg of FeTe (the detailed synthetic method of FeTe was described in the Supporting Information) was uniformly dispersed in 80 mL CH_3OH via ultrasound 1 h. 3.7 g of 2-MeIM and 1.68 g of $Zn(NO_3)_2 \cdot 6H_2O$ were separately added to 80 mL CH_3OH via ultrasound 10 min. The two solutions of equal mass were poured

into the FeTe solutions and mechanically stirred for 24 h. The products (denoted as FeTe@ZIF-8) were obtained by filtration with CH_3OH. The FeTe@ZIF-8 was carbonized at 950 °C for 3 h (5 °C/min) under Ar. The corresponding name was Fe_Z-NC.

Preparation of Fe_{DZ}-NC-x electrocatalysts. The 10 mg, 50 mg, 100 mg, 200 mg, 300 mg of FeTe was uniformly dispersed in 80 mL CH_3OH via ultrasound 1 h, respectively. 3.7 g of 2-MeIM and 1.68 g of $Zn(NO_3)_2 \cdot 6H_2O$ were separately added to 80 mL CH_3OH via ultrasound 10 min. The two solutions of equal mass were poured into the above each FeTe solutions and mechanically stirred 24 h. The all products were filtered by CH_3OH. The obtained five FeTe@ZIF-8 was separate added to the 80 mL tris-buffer media (pH=8.5) via ultrasound 30 min. 100 mg of dopamine was poured into the five solutions, respectively. The reaction products (denoted as polydopamine (PDA)@FeTe@ZIF-8) were obtained by filtration with deionized water after magnetic stirring for 12 h. Those PDA@FeTe@ZIF-8 was carbonized at 950 °C for 3 h (5 °C/min) in Ar. The final samples were denoted as Fe_{DZ}-NC-10, Fe_{DZ}-NC-50, Fe_{DZ}-NC-100 (Fe_{DZ}-NC), Fe_{DZ}-NC-200, Fe_{DZ}-NC-300.

Preparation of Fe_L-NC catalyst. The synthesis step was the same as the synthesis Fe_{DZ}-NC step. The $FeCl_3 \cdot 6H_2O$ was replaced with the same mole of iron as 100 mg FeTe. The product obtained after carbonization was denoted as Fe_L-NC.

Preparation of N-C electrocatalysts. The synthesis step was the same as the synthesis Fe_{DZ}-NC, but no FeTe was added. The product obtained after carbonization was denoted as N-C.

Preparation of the electrode. For the electrode, the catalyst (5 mg) or commercial Pt/C (5 mg) was dispersed in CH_3CH_2OH (100 µL), deionized water (300 µL) and 5% Nafion solution (100 µL) to sonicate to form a uniform solution, respectively. Then 8 mL solution was applied to the shiny glassy

carbon electrode and dried it.

Material Characterizations. The morphologies feature of the materials was observed by SEM (SU8000), TEM (JEOL JEM-200CX) and HRTEM (FEI Tecnai G2 F20). The crystalline composition of as-obtained materials was investigated by powder X-ray diffraction (XRD) (Rigaku 3KW D/MAX2200V PC, Kα radiation) over the range 10-90° (2θ). X-ray photoelectron spectroscopic (XPS) measurements were recorded by the (Mg Ka (1253.6 eV) radiation) Perkin-Elmer PHI 5000C ESCA system. N_2-adsorption/desorption measurements were conducted in a MicroActive ASAP 2460 analyzer instrument under 77 K. The specific surface area (SSA) of the materials was estimated by the Multi-point BET method. The pore size distribution for the materials was recorded by the Density Functional Theory (DFT) method.

Electrochemical measurements. All the electrochemical characterizations were carried out on CHI 760E electrochemical workstation (Shanghai Chenhua Instrument Co.) with the three electrodes system. A rotating disc of glassy carbon electrode (D ¼ 5 mm) represented the working electrode. A Pt foil represented counter electrode and an Ag/AgCl electrode represented reference electrode. In 0.1 mol L^{-1} O_2 or N_2 saturated KOH aqueous media, the Cyclic voltammetry (CV) curves were measured in 100 mV/s. Linear Sweep Voltammetry (LSV) was tested in 0.1 mol L^{-1} O_2 saturated KOH media under different revolutions with 10 mV/s. The long-term stability was tested using chronoamperometry by recording ORR current for 12 h at -0.25 V and 400 rpm. The methanol-tolerant were investigated in 0.1 mol L^{-1} O_2 saturated KOH aqueous media, and 5 mL CH_3OH was added and rotated for 1h. Moreover, the current was recorded at -0.25V and 1600 rpm. The RRDE was tested by using the rotating ring disk electrode with platinum ring. The diameter of glassy carbon disk was 5.4 mm.

Kinetic current density was recorded by Koutecky-Levich equation at 0.2 V, 0.3 V, 0.4 V, 0.5 V and 0.6 V potentials [59] (A1):

$$\frac{1}{J} = \frac{1}{B\omega^{0.5}} + \frac{1}{J_K} \qquad (A1)$$

where J_K stands for the kinetic current, ω stands for the electrode rotation rate. B stands for the slope of the Koutecky-Levich equation [60] (A2):

$$B = 0.2nF\upsilon^{-\frac{1}{6}}Co_2(Do_2)^{-\frac{2}{3}} \qquad (A2)$$

The n stands for the electron transfer capability, F stands for the Faraday's constant (F=96485 C mol^{-1}), υ stands for the dynamic viscosity of 0.1 mol L^{-1} KOH (υ=0.01 cm^2 s^{-1}), Co_2 stands for the concentration of oxygen (1.2×10^{-3} mol L^{-1}), Do_2 stands for the diffusion coefficient of oxygen (1.9×10^{-5} cm s^{-1}). The constant for the rotating speed (rpm) is 0.2.

The yield of hydrogen peroxide ($H_2O_2\%$) is obtained by the rotating ring disk electrode in ORR equipment and CHI 760E electrochemical workstation. The yield of H_2O_2 and the electron transfer capability (n) were recorded with the two equations [61, 62] (A3) (A4):

$$H_2O_2(\%) = \frac{\frac{200I_R}{N}}{I_D + \frac{I_R}{N}} \qquad (A3)$$

$$n = \frac{4I_D}{I_D + \frac{I_R}{N}} \qquad (A4)$$

The I_R and I_D stand for ring current and disk current, and N stands for the ring collection efficiency (37%).

■ RESULTS AND DISCUSSION

The characterization of catalysts

The preparation of the Fe_{DZ}-NC catalysts with hierarchical structure was illustrated in Fig 1. The FeTe (Fig S1) [58] were synthesized by the hydrothermal method, serving as a sacrificial

template trapped in the cavities of ZIF-8 to form the FeTe@ZIF-8 complexes. As presented the Figure S2a-b, the as-prepared FeTe@ZIF-8 shared the similar morphology with the ZIF-8, which was not affected by the introduction of FeTe. Besides morphology, the bulk crystal structure of FeTe@ZIF-8 also remained the same as the ZIF-8 by XRD [63,64]. Simultaneously, the characteristic peak of FeTe was identified in the XRD patterns of FeTe@ZIF-8[63,64], indicating that FeTe was dispersed in ZIF-8. Subsequently, the polydopamine (PDA) membrane was coated over the surface of the FeTe@ZIF-8 by self-assembly of dopamine.

The morphology structures of pyrolyzed materials were investigated using SEM and TEM. As was shown in the Fig. 2a-c, the SEM and TEM images of the Fe_{DZ}-NC displayed pseudo-octahedral structure with hollow mesoporous structure. The average size of the particle was about 56 nm with inner diameter (Fig. S2 d). The outer carbon layer exhibited amorphous structure with thickness of 8 nm compared to the Fe_L-NC materials (Fig. S3 a-b). It revealed that both the evaporation of Zn and Te could etch the carbon frameworks to form more voids inside MOFs during the pyrolysis process. However, without the dopamine coating, the Fe_Z-NC materials derived from carbonization of FeTe@ZIF-8 collapsed (Fig. S4). This is because the dopamine coating on the surface of the ZIF-8 could form highly graphitic carbon layer to retain the original structure after the carbonization. The Fe_{DZ}-NC materials was further characterized by HRTEM (Fig. 2c). No nanoparticles of iron were detected, indicating that no agglomeration of iron. Additionally, the energy-dispersive X-ray spectroscopy (EDS) mapping of the Fe_{DZ}-NC materials (Fig. 2d) showed the Fe, N, C elements were uniform distributed in the carbon frameworks.

The crystal structure of as-obtained materials was investigated by XRD. As shown in Fig.

3a, the only hump peaks at 25° and 43° correspond to the amorphous carbon structure [65,66] and indicated the totally removal of Te which was in consistent with HRTEM results. At the same time, the XPS spectrum of for the Fe_{DZ}-NC and Fe_Z-NC before pyrolysis show obvious zinc and tellurium peaks, but the carbonized samples do not show zinc and tellurium peaks (Fig. S5 and Table S1). When FeTe was replaced by $FeCl_3$, peaks indexed to Fe, Fe_3C, and Fe_3O_4 were found in Fig. 3a. Moreover, the Fe_3C would emerge without extra N providing by dopamine. It was worthwhile that FeTe could only decompose and released Fe at high temperature (Fig. S6 c). This was consistent with the HRTEM images that no iron agglomeration was formed. This proved that the evaporation of Te was conducive to the formation of the uniformly dispersed FeN_x sites, thus inhibiting the formation of iron oxide. In addition, the relative diffraction
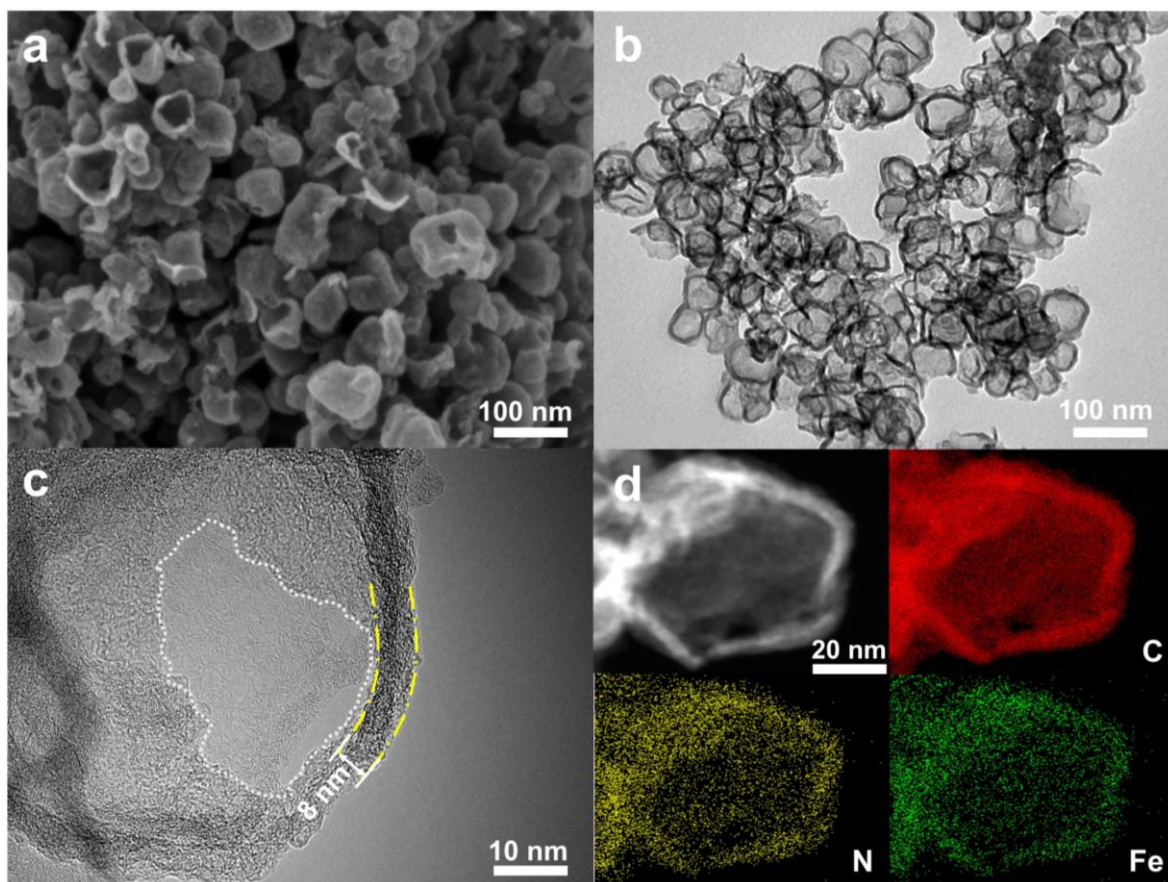

Fig 2. (a) SEM, (b) TEM, (c) HRTEM, (d) HAADF/STEM images and the corresponding EDS elemental mapping (C, N

and Fe) of Fe_{DZ}-NC.

intensity of the Fe_3C peak increased with the increased Fe content in the Fe_{DZ}-NC materials (Fig. S6 b, Fig.S7). This is because the excessive Fe made it difficult for C atoms inside the nanocrystals to diffuse to the outer surface, hence forming more Fe_3C phases [67-69].

The Raman spectrum was also used to characterize the graphitic level of the pyrolyzed materials. The bands of D and G represent the degrees of graphitization and disorder or defects of the material structure respectively [70-71]. The intensity ratio of I_D/I_G was positively related to the defect degree of the graphitized carbon [72-73]. The integral area values of D peak and G peak were displayed in Table S2. The Raman spectra of the Fe_{DZ}-NC materials showed a higher disorder degree with a higher I_D/I_G (1.85) than those of the Fe_Z-NC and Fe_L-NC materials (Fig. 3b, Fig. S8, Table S2). Obviously, the evaporation of Te led to more plentiful defects.

The evaporation of Te also gave rise to porous structure which was also investigated by N_2-adsorption/desorption measurements (Fig. 3c, Fig. S9 a). Typical IV isotherms were found for Fe_{DZ}-NC, Fe_Z-NC and Fe_L-NC showing a combination of both micropores and mesopores. The specific surface area (SSA) of the materials was estimated by the Multi-point BET method. The textural characteristics of the materials were showed in Table S3. The specific surface area of Fe_{DZ}-NC was higher than those of the Fe_L-NC, Fe_Z-NC (Fig. 3d), which was mainly attributed to the preservation of the ZIF-derived porous frameworks and polydopamine-derived mesopore structure. The high surface area could facilitate the dispersion of active species and promote catalytic performance. However, the specific surface area of the Fe_{DZ}-NC materials tended to decrease with the increase of Fe content, which was caused by the accumulation of excessive Fe_3C during pyrolysis. The pore size distribution for the materials (Fig. S9 b) was

analyzed by the DFT method. The pore diameter and porosity of Fe_{DZ}-NC represented the micro-mesoporous structures (Fig. S10). The highest total pore volume dominating with mesopore volume was found for Fe_{DZ}-NC which could provide a buffer for the electrolytes. The N_2 sorption results showed that Fe_{DZ}-NC owned hierarchically porous structure with large surface area which enabled the well exposure of active species and effective electrolytes diffusion.
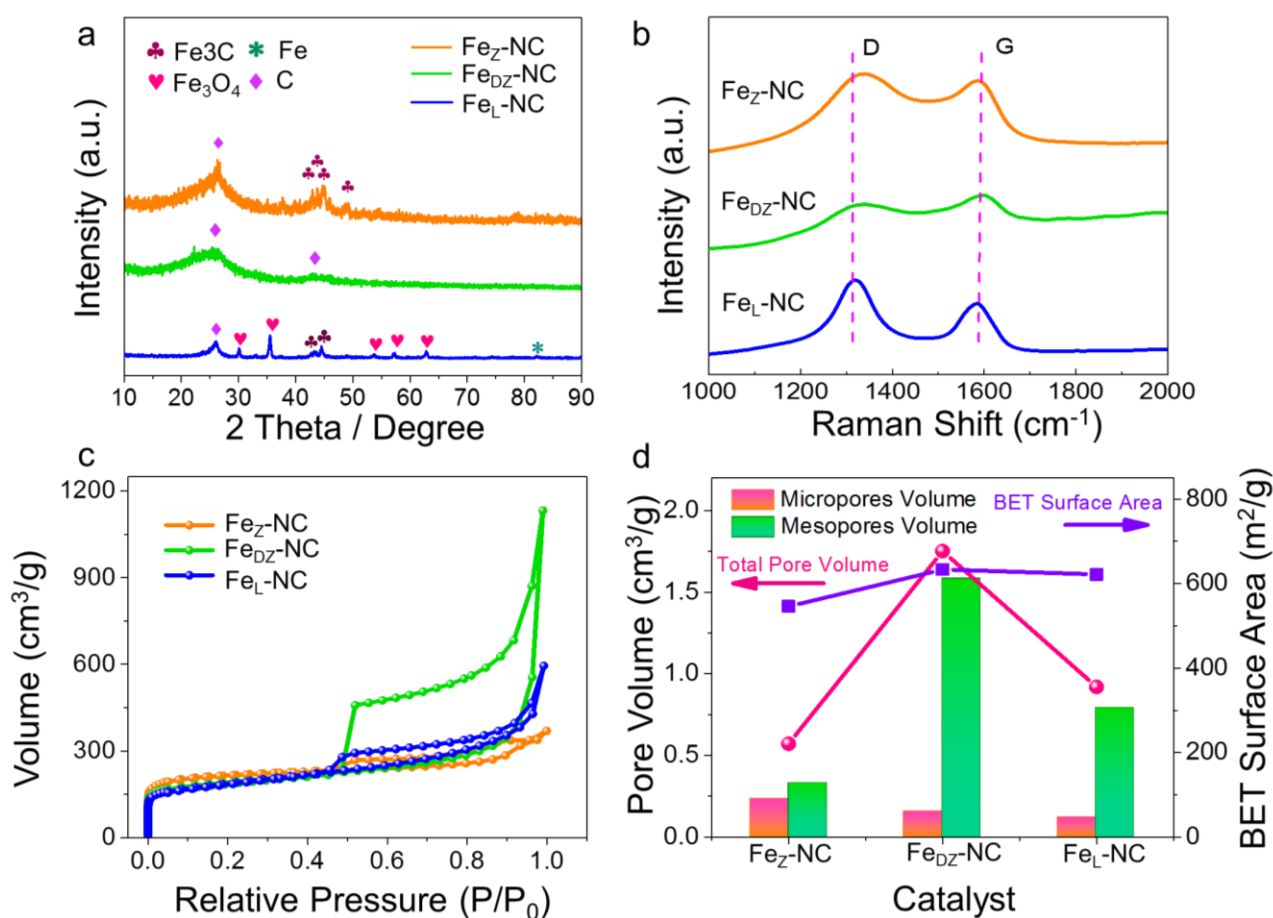
Fig 3. (a) XRD patterns, (b) Raman spectra, (c) N_2 adsorption-desorption isotherms, and (d) Plots of BET surface area and pore volume of various Fe-N-C materials.

The XPS was used to measure element compositions and chemical valence states of the pyrolyzed materials. The atomic ratio of element signals of different materials was shown in Table S4 and the 0.2%, 0.59%, and 0.57% Fe was found for Fe_Z-NC, Fe_{DZ}-NC, and Fe_L-NC,

respectively. The iron content was further tested by ICP, and the results are shown in Table S5 From the obtained spectrum, elements signal of Fe, N and C could be clearly observed on Fe_{DZ}-NC materials, which was also consistent with element mapping results. The C 1s spectrum in the materials was divided into four types (C-C (~284.5 eV), C-N (~285.8 eV), C=N (~287.2 eV), C=O (~287.9eV)) by the peak-differentiating and imitating (Fig. 4a, Fig. S11 a, Fig. S12 b). The C-C peaks represented the graphitized carbon. The C-N and C=N peaks suggested that the N atoms were inserted into the basal plane of graphitic carbon. The incorporation of N dopants had a higher electronegativity with the adjacent C atoms, which facilitated the adsorption and reduction of O_2, thereby improving the ORR catalytic performance [74-76]. High resolution N 1s spectrum (Fig. 4b, Fig. S11 b, Fig. S12 b) of the materials revealed the existence of pyridinic N (N-6 at ~398.6 eV), Fe-N (~399.4 eV), pyrrolic N (N-5 at ~400.1 eV), graphitic N (N-G at ~401.2 eV) and oxidized N (N-O at ~402.1 eV) nitrogen species. The doping of nitrogen in carbon materials had a variety of configurations, and the different doping configurations had different effects on the catalytic performance[77-78]. Graphitic N was the N atom linked to three sp^2 carbon atoms, which was favorable to exalting the limiting current density. The area ratio of N species of the materials was summarized in Table S6. The nitrogen content of Fe_{DZ}-NC reached 6.22% with a graphitic N content of 2.45%, which was significantly higher than others. The high content of graphite N was favorable for electrocatalysis. Simultaneously, the content of Fe-N species in the Fe_{DZ}-NC material was higher than those of other Fe-N-C materials. This suggested that the Fe_{DZ}-NC material could form more FeN_x active species. In addition, the relative composition of the high-resolution Fe 2p spectrum were Fe (0), Fe $2p_{3/2}$, Fe $2p_{1/2}$ in the materials (Fig. S13). The peak at 708 eV

corresponded to Fe (0) which could not be found in Fe$_{DZ}$-NC materials. The noticeable peaks at 712.6 and 725.0 eV corresponded to Fe (III) species [79-84]. The peaks at 710.3 eV and 723.1 eV corresponded to Fe (II) species [85-87]. The Fe ions with different valence states contributed to the formation of FeN$_x$ active species in the Fe$_{DZ}$-NC materials, which was beneficial to the electrocatalysis.
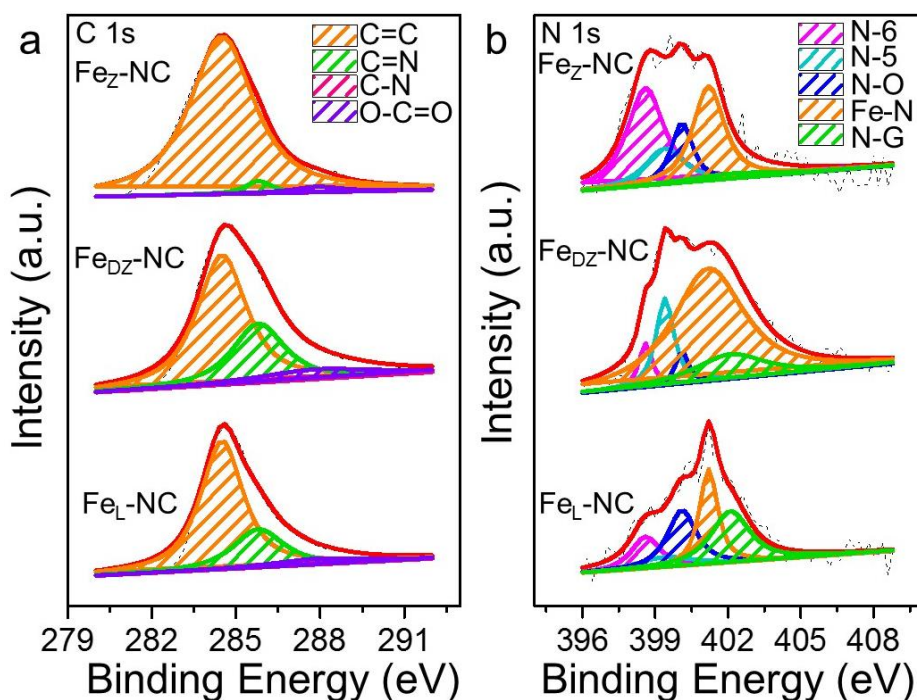

Fig 4. (a) C 1s spectra and (b) N 1s spectra of various Fe-N-C materials.

Electrochemical property of catalysts for ORR

The ORR catalytic property of the catalytic materials was firstly tested by CV curves in 0.1 M KOH media (Fig. 5a, Fig. S14). The redox peak of CV curves was not observed in N$_2$-saturated conditions, while the cathodic redox peak potentials were observed in O$_2$-saturated conditions. The Fe$_{DZ}$-NC catalyst revealed the highest peak potential (~0.72V), which indicated a more positive ORR performance than any other catalysts. The ORR performances of the materials were further observed by LSV tests using RDE at a sweep rate of 10 mV/s (Fig. 5b). The Fe$_{DZ}$-NC displayed more positive ORR property with the onset potential of 0.98 V. The half-wave

potential was 0.863 V with limit current density of 6.23 mA/cm^2, which was superior to the Pt/C and previously reported Fe-N-C materials (Fig. 5c, Table S7). Moreover, it could be calculated that the Tafel slope (Fig. 5d) of Fe$_{DZ}$-NC was 72 mV /dec, which was lower than that of precious Pt/C (96 mV/dec). In addition, compared
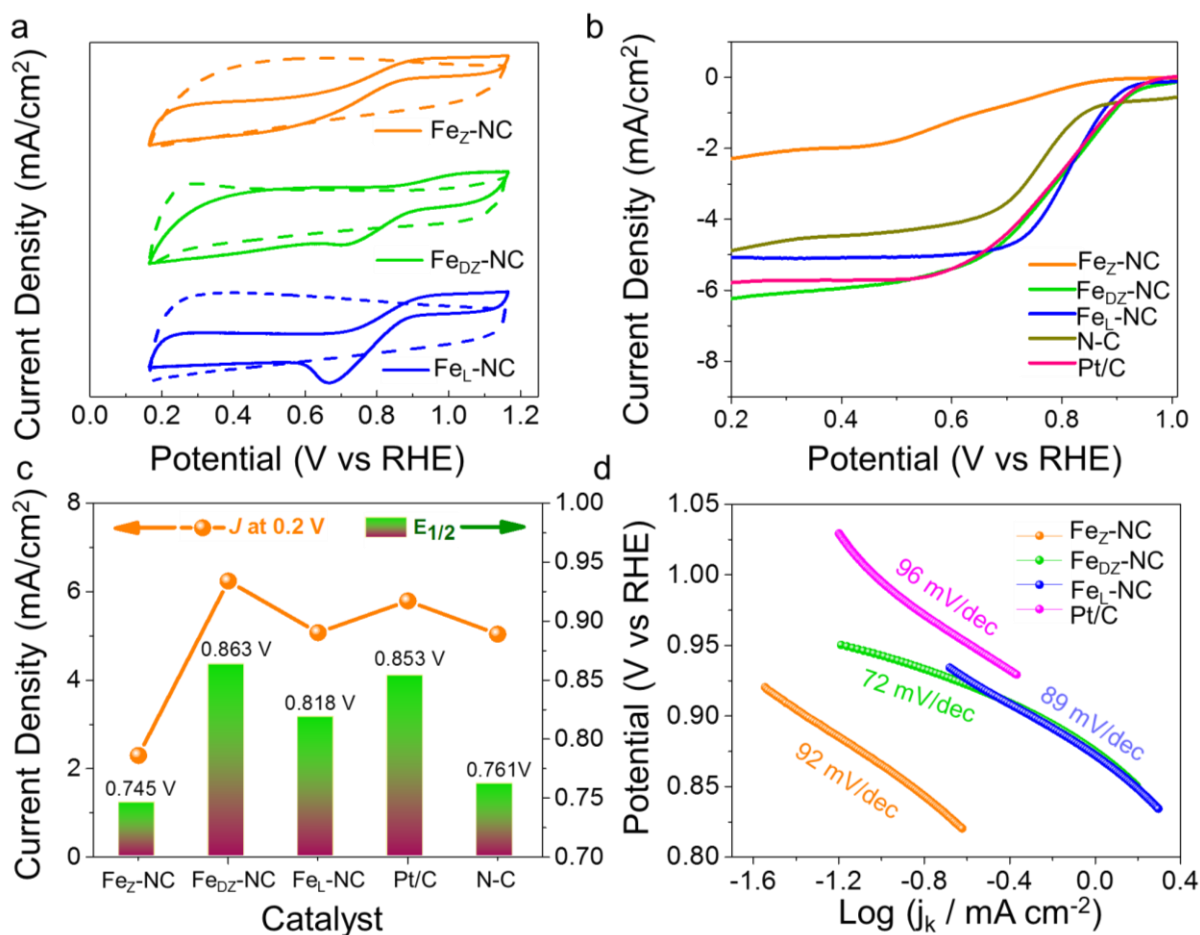
Fig 5. (a) CV curves in N$_2$ (dotted line) or O$_2$ (solid line) saturated 0.1 M KOH solution (b) LSV curves for various Fe-N-C materials; (c) Plots of current density (J) and half wave potential (E$_{1/2}$) for various catalysts; (d) Tafel plots of various Fe-N-C materials and Pt/C.

to the Fe$_Z$-NC materials, the Fe$_{DZ}$-NC materials had the PDA and ZIF-8-derived porous structure to form the higher surface area and more appropriately interconnected 3D network pore structure, which could effectively facilitate the mass transfer capability of the electrolyte, shorten the ion diffusion paths. Furthermore, the electrocatalytic properties of the materials in

0.5 M H_2SO_4 solution and the effect of Fe content were also investigated in alkaline media by the LSV tests. In Fig. S15, the Fe-NC materials exhibited better electrocatalytic performance in alkaline media than the acidic media. When the content of iron was low, the ability of the active site in the material was insufficient and provided higher initial potential and half wave potential, so that the limit current was difficult to achieve equilibrium. However, the higher Fe content would lead to a decline in catalytic performance, possibly due to the aggregation of Fe_3C.

The performance of various Fe-N-C materials and precious Pt/C catalysts were further investigated by RDE measurements at 400 to 2500 rpm rotation rates. The electron transfer capability (n) were calculated at different rotation rates by the Koutecky-Levich (K-L) equation. LSV curves and K-L plots of all materials at 400 to 2500 rpm rotation rates were shown in Fig. S16-24. The linearity and parallelism of the K-L plots revealed a first-order reaction kinetics [88-89]. The n values of Fe_{DZ}-NC were close to 4 in the potential ranges from 0.2 to 0.6 V $_{RHE}$, which was superior to n values of the series of synthetic materials, signifying an optimum four-electron ORR transfer pathway. Simultaneously, the electron transfer numbers were also investigated by the rotating ring-disk electrode (RRDE) measurement. As shown in Fig. 6a and Fig. S25, the n value of the Fe_{DZ}-NC catalyst was close to 4 in the voltage ranges from 0.2 to 0.6 V $_{RHE}$, and the yield of H_2O_2 was below 3% (Fig. 6b), which were both superior to the Pt/C catalyst and other Fe-NC catalysts. The calculated results coincided with those of K-L equation, verifying an optimum four-electron ORR transfer pathway.

The methanol-tolerant and long-term durability of materials were also quite important in the ORR property. The methanol-tolerant and long-term durability were investigated via the

current versus time (I-t) chronoamperometric measurements. As shown in Fig. 6c and Fig. S26, when 5 mL CH_3OH was injected into the 0.1 mol L^{-1} O_2-saturated KOH media at 400 s, the Fe_{DZ}-NC and other materials showed a slight current movement. In contrast, the precious Pt/C catalyst showed an abrupt drop in current density. This suggested that Fe_{DZ}-NC had a better performance for the ORR with the methanol poisoning. In addition, the Fe_{DZ}-NC catalyst exhibited an excellent stability in the 0.1 mol L^{-1} O_2-saturated KOH media at 0.7 V $_{RHE}$. After the 12 h test, the Fe_{DZ}-NC catalyst could still maintain 97% of its initial current density, whereas the Pt/C catalyst lost its current density

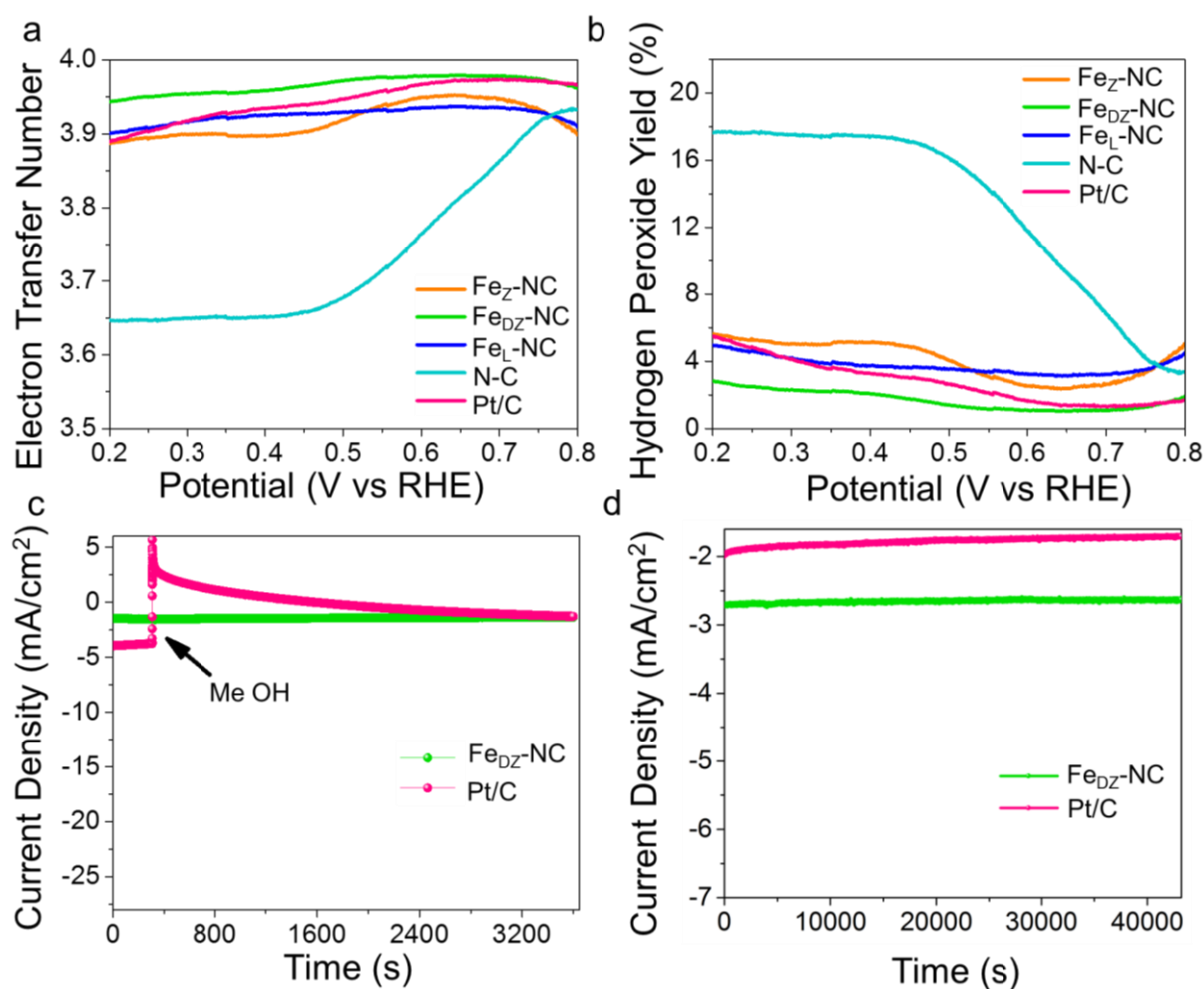Fig 6. (a) Plots of electron transfer numbers for various Fe-N-C materials in the RRDE measurement in the 0.1 mol L^{-1} O_2-saturated KOH media and 1600 rpm; (b) plots of H_2O_2 yield of various Fe-N-C materials in the RRDE measurement in the

16

0.1 mol L^{-1} O$_2$-saturated KOH media and 1600 rpm; (c) methanol tolerance curves of Fe$_{DZ}$-NC materials and Pt/C in the 0.1 mol L^{-1} O$_2$-saturated KOH media at 0.7 V $_{RHE}$ and 1600 rpm; and (d) current *versus* time (I–t) chronoamperometric curves of Fe$_{DZ}$-NC materials and Pt/C in the 0.1 mol L^{-1} O$_2$-saturated KOH media at 0.7 V $_{RHE}$ and 400 rpm.

by 16% due to severe degradation (Fig. 6d, Fig. S27.). The excellent stability of Fe$_{DZ}$-NC could be attributed to the FeN$_x$ active species being embedded into carbon matrix and covered with highly graphitic layer, which could provide dual-protection for active species. All the above-mentioned properties demonstrated that the Fe$_{DZ}$-NC material was an ideal electrocatalyst for ORR in alkaline media.

■ CONCLUSION

In summary, we have successfully synthesized the Fe, N-doped porous carbon architectures from FeTe-trapped ZIF-8 coated with polydopamine by heat treatment. During the carbonization process, the evaporation of Te could inhibit the formation of iron oxides, promote the formation of more FeN$_x$ active species, and facilitate the formation of mesoporous structure to accelerate mass transfer and improve the approachability of active species. Simultaneously, the mixture of ZIF-8 and the extra N resource PDA were carbonized to get abundant graphitic N to raise the ORR catalytic performance. The newly synthesized Fe$_{DZ}$-NC catalyst exhibited the excellent ORR activity among various Fe-N-C materials. Remarkably, the methanol-tolerant and long-term durability of Fe$_{DZ}$-NC were even better than the precious Pt/C catalyst. Hence, the study has proposed a new method to improve mass transfer in the Fe-N-C catalysis system by using metal tellurides to break the microcavity of ZIF-8 to create rich mesoporous structure, and opened new avenues for the design of the highly uniformly dispersed non-noble metal-nitrogen sites catalysts for ORR.

ASSOCIATED CONTENT

Supporting information

The Supporting Information is available free of charge on the ACS Publications website.

Materials, Synthesis of FeTe, Structural characterization, Electrochemical characterization, SEM images, TEM images, XRD patterns, Raman spectra, BET information, XPS information, CV curves, LSV curves, K-L plots, EDS mapping and Comparison of ORR performance with another electrocatalysts (PDF).

AUTHOR INFORMATION

Corresponding Authors

* E-mail: dszhang@shu.edu.cn; Tel: +86 21 66137152.

CONFLICTS OF INTEREST

There are no conflicts to declare.

ACKNOWLEDGMENTS

REFERENCES

(1) Dunn, B.; Kamath, H.; Tarascon, J. M., Electrical Energy Storage for the Grid: A Battery of Choices. Science 2011, 334, 928-935.

(2) Chu, S.; Majumdar, A., Opportunities and Challenges for a Sustainable Energy Future. Nature 2012, 488, 294-303.

(3) Ong, B. C.; Kamarudin, S. K.; Basri, S., Direct liquid fuel cells: A review. Int J Hydrog Energy 2017, 42, 10142-10157.

(4) An, L.; Zhao, T. S., Transport phenomena in alkaline direct ethanol fuel cells for sustainable energy production. J. Power Source 2017, 341, 199-211.

(5) Muneeb, O.; Do, E.; Tran, T.; Boyd, D.; Huynh, M.; Ghosn, G.; Haan, J. L., A direct ascorbate fuel cell with an anion exchange membrane. J. Power Source 2017, 351, 74-78.

(6) Kwak, D. H.; Han, S. B.; Kim, D. H.; Won, J. E.; Park, K. W., Amino acid-derived non-precious catalysts with excellent electrocatalytic performance and methanol tolerance in oxygen reduction reaction. Appl Catal B: Environ 2018, 238, 93-103.

(7) Li, C. H.; Liu, H. X.; Yu, Z. Y., Novel and multifunctional inorganic mixing salt-templated 2D ultrathin Fe/Co-N/S-carbon nanosheets as effectively bifunctional electrocatalysts for Zn-air batteries. Appl Catal B: Environ 2019, 241, 95-103.

(8) Kwak, D.-H.; Han, S.-B.; Lee, Y.-W.; Park, H.-S.; Choi, I.-A.; Ma, K.-B.; Kim, M.-C.; Kim, S.-J.; Kim, D.-H.; Sohn, J.-I.; Park, K.-W., Fe/N/S-doped mesoporous carbon nanostructures as electrocatalysts for oxygen reduction reaction in acid medium. Appl Catal B: Environ 2017, 203, 889-898.

(9) Zubiaur, A.; Job, N., Streamlining of the synthesis process of Pt/carbon xerogel electrocatalysts with high Pt loading for the oxygen reduction reaction in proton exchange membrane fuel cells applications. Appl Catal B: Environ 2018, 225, 364-378.

(10) Nie, Y.; Li, L.; Wei, Z., Recent advancements in Pt and Pt-free catalysts for oxygen reduction reaction. Chem. Soc. Rev 2015, 44, 2168-2201.

(11) Bu, L.; Zhang, N.; Guo, S.; Zhang, X.; Li, J.; Yao, J.; Wu, T.; Lu, G.; Ma, J.-Y.; Su, D.; Huang,

X., Biaxially strained Pt Pb/Pt core/shell nanoplate boosts oxygen reduction catalysis. Science 2016, 354, 1410-1414.

(12) He, D.; Zhang, L.; He, D.; Zhou, G.; Lin, Y.; Deng, Z.; Hong, X.; Wu, Y.; Chen, C.; Li, Y., Amorphous nickel boride membrane on a platinum-nickel alloy surface for enhanced oxygen reduction reaction. Nat. Commun 2016, 7, 12362.

(13) Li, M.; Zhao, Z.; Cheng, T.; Fortunelli, A.; Chen, C.-Y.; Yu, R.; Zhang, Q.; Gu, L.; Merinov, B. V.; Lin, Z.; Zhu, E.; Yu, T.; Jia, Q.; Guo, J.; Zhang, L.; Goddard, W. A., III; Huang, Y.; Duan, X., Ultrafine jagged platinum nanowires enable ultrahigh mass activity for the oxygen reduction reaction. Science 2016, 354, 1414-1419.

(14) Xia, W.; Mahmood, A.; Liang, Z.; Zou, R.; Guo, S., Earth-Abundant Nanomaterials for Oxygen Reduction. Angew. Chem., Int. Ed 2016, 55, 2650-2676.

(15) Wang, J.; Huang, Z.; Liu, W.; Chang, C.; Tang, H.; Li, Z.; Chen, W.; Jia, C.; Yao, T.; Wei, S.; Wu, Y.; Li, Y., Design of N-Coordinated Dual-Metal Sites: A Stable and Active Pt-Free Catalyst for Acidic Oxygen Reduction Reaction. J. Am. Chem. Soc 2017, 139, 17281-17284.

(16) Wang, R.; Yan, T.; Han, L.; Chen, G.; Li, H.; Zhang, J.; Shi, L.; Zhang, D., Tuning the dimensions and structures of nitrogen-doped carbon nanomaterials derived from sacrificial g-C_3N_4/metal–organic frameworks for enhanced electrocatalytic oxygen reduction. J. Mater. Chem. A 2018, 6, 5752-5761.

(17) Liu, P.; Liu, Y.; Jiang, J.; Ashraf, S.; Wu, X.; Han, G.; Gao, J.; Zhang, K.; Li, B., Co-, Fe-, and N-Modified Carbon Composites for Excellent Catalytic Performances toward Electrochemical Reduction Reaction. ACS Sustainable Chem. Eng. 2019, 7, 8744-8754.

(18) Guo, J.; Cheng, Y.; Xiang, Z., Confined-Space-Assisted Preparation of Fe_3O_4-Nanoparticle-

Modified Fe-N-C Catalysts Derived from a Covalent Organic Polymer for Oxygen Reduction. ACS Sustainable Chem. Eng. 2017, 5, 7871-7877.

(19) Yan, T.; Liu, J.; Lei, H.; Shi, L.; An, Z.; Park, H. S.; Zhang, D., Capacitive deionization of saline water using sandwich-like nitrogen-doped graphene composites via a self-assembling strategy. Environ Sci: Nano 2018, 5, 2722-2730.

(20) Han, J.; Shi, L.; Yan, T.; Zhang, J.; Zhang, D., Removal of ions from saline water using N, P co-doped 3D hierarchical carbon architectures via capacitive deionization. Environ Sci: Nano 2018, 5, 2337-2345.

(21) Wang, H.; Yan, T.; Shi, L.; Chen, G.; Zhang, J.; Zhang, D., Creating Nitrogen-Doped Hollow Multiyolk@Shell Carbon as High Performance Electrodes for Flow-Through Deionization Capacitors. ACS Sustainable Chem. Eng. 2017, 5, 3329-3338.

(22) Li, J.; Chen, M.; Cullen, D. A.; Hwang, S.; Wang, M.; Li, B.; Liu, K.; Karakalos, S.; Lucero, M.; Zhang, H.; Lei, C.; Xu, H.; Sterbinsky, G. E.; Feng, Z.; Su, D.; More, K. L.; Wang, G.; Wang, Z.; Wu, G., Atomically dispersed manganese catalysts for oxygen reduction in proton-exchange membrane fuel cells. Nat. Catal 2018, 1, 935-945.

(23) Hu, E. L.; Yu, X. Y.; Chen, F.; Wu, Y. D.; Hu, Y.; Lou, X. W., Graphene Layers-Wrapped Fe/Fe_5C_2 Nanoparticles Supported on N-doped Graphene Nanosheets for Highly Efficient Oxygen Reduction. Adv. Energy Mater 2018, 8, 1702476.

(24) Li, Y. L.; Jia, B. M.; Fan, Y. Z.; Zhu, K. L.; Li, G. Q.; Su, C. Y., Bimetallic Zeolitic Imidazolite Framework Derived Carbon Nanotubes Embedded with Co Nanoparticles for Efficient Bifunctional Oxygen Electrocatalyst. Adv. Energy Mater 2018, 8, 1702048.

(25) Zhu, C.; Shi, Q.; Xu, B. Z.; Fu, S.; Wan, G.; Yang, C.; Yao, S.; Song, J.; Zhou, H.; Du, D.;

Beckman, S. P.; Su, D.; Lin, Y., Hierarchically Porous M-N-C (M = Co and Fe) Single-Atom Electrocatalysts with Robust MNx Active Moieties Enable Enhanced ORR Performance. Adv. Energy Mater 2018, 8, 1801956.

(26) Guan, B. Y.; Lu, Y.; Wang, Y.; Wu, M.; Lou, X. W. D., Porous Iron-Cobalt Alloy/Nitrogen-Doped Carbon Cages Synthesized via Pyrolysis of Complex Metal-Organic Framework Hybrids for Oxygen Reduction. Adv. Funct. Mater 2018, 28, 1706738.

(27) Lee, J.-S. M.; Sarawutanukul, S.; Sawangphruk, M.; Horike, S., Porous Fe-N-C Catalysts for Rechargeable Zinc-Air Batteries from an Iron-Imidazolate Coordination Polymer. ACS Sustainable Chem. Eng. 2019, 7, 4030-4036.

(28) Jahan, M.; Bao, Q.; Loh, K. P., Electrocatalytically Active Graphene-Porphyrin MOF Composite for Oxygen Reduction Reaction. J. Am. Chem. Soc 2012, 134, 6707-6713.

(29) Zhang, H.; Hwang, S.; Wang, M.; Feng, Z.; Karakalos, S.; Luo, L.; Qiao, Z.; Xie, X.; Wang, C.; Su, D.; Shao, Y.; Wu, G., Single Atomic Iron Catalysts for Oxygen Reduction in Acidic Media: Particle Size Control and Thermal Activation. J. Am. Chem. Soc 2017, 139, 14143-14149.

(30) Jiao, L.; Wan, G.; Zhang, R.; Zhou, H.; Yu, S. H.; Jiang, H. L., From Metal-Organic Frameworks to Single-Atom Fe Implanted N-doped Porous Carbons: Efficient Oxygen Reduction in Both Alkaline and Acidic Media. Angew. Chem 2018, 57, 8525-8529.

(31) Chen, Y.; Ji, S.; Zhao, S.; Chen, W.; Dong, J.; Cheong, W.-C.; Shen, R.; Wen, X.; Zheng, L.; Rykov, A. I.; Cai, S.; Tang, H.; Zhuang, Z.; Chen, C.; Peng, Q.; Wang, D.; Li, Y., Enhanced oxygen reduction with single-atomic-site iron catalysts for a zinc-air battery and hydrogen-air fuel cell. Nat. Commun 2018, 9, 5422.

(32) Xu, X.; Xia, Z.; Zhang, X.; Sun, R.; Sun, X.; Li, H.; Wu, C.; Wang, J.; Wang, S.;

Sun, G., Atomically dispersed Fe-N-C derived from dual metal-organic frameworks as efficient oxygen reduction electrocatalysts in direct methanol fuel cells. Appl Catal B: Environ 2019, 259, 118042.

(33) Ko, Y.-J.; Kim, H.-G.; Seid, M. G.; Cho, K.; Choi, J.-W.; Lee, W.-S.; Hong, S. W., Ionic-Liquid-Derived Nitrogen-Doped Carbon Electrocatalyst for Peroxide Generation and Divalent Iron Regeneration: Its Application for Removal of Aqueous Organic Compounds. ACS Sustainable Chem. Eng. 2018, 6, 14857-14865.

(34) Xu, J.; Wu, C.; Yu, Q.; Zhao, Y.; Li, X.; Guan, L., Ammonia Defective Etching and Nitrogen-Doping of Porous Carbon toward High Exposure of Heme-Derived Fe-N-x Site for Efficient Oxygen Reduction. ACS Sustainable Chem. Eng. 2018, 6, 551-560.

(35) Ye, G.; Zhao, K.; He, Z.; Huang, R.; Liu, Y.; Liu, S., Fe-N-x Sites Enriched Carbon Micropolyhedrons Derived from Fe-Doped Zeolitic Imidazolate Frameworks with Reinforced Fe-N Coordination for Efficient Oxygen Reduction Reaction. ACS Sustainable Chem. Eng. 2018, 6, 15624-15633.

(36) Li, J.; Chen, J.; Wan, H.; Xiao, J.; Tang, Y.; Liu, M.; Wang, H., Boosting oxygen reduction activity of Fe-N-C by partial copper substitution to iron in Al-air batteries. Appl Catal B: Environ 2019, 242, 209-217.

(37) Lee, S. H.; Kim, J.; Chung, D. Y.; Yoo, J. M.; Lee, H. S.; Kim, M. J.; Mun, B. S.; Kwon, S. G.; Sung, Y.-E.; Hyeon, T., Design principle of Fe-N-C electrocatalysts: How to optimize multimodal porous structures? J. Am. Chem. Soc 2019, 141, 2035-2045.

(38) Mun, Y.; Kim, M. J.; Park, S. A.; Lee, E.; Ye, Y.; Lee, S.; Kim, Y. T.; Kim, S.; Kim, O. H.; Cho, Y. H.; Sung, Y. E.; Lee, J., Soft-template synthesis of mesoporous non-precious metal catalyst with Fe-

N-X/C active sites for oxygen reduction reaction in fuel cells. Appl Catal B: Environ 2018, 222, 191-199.

(39) Seh, Z. W.; Kibsgaard, J.; Dickens, C. F.; Chorkendorff, I. B.; Norskov, J. K.; Jaramillo, T. F., Combining theory and experiment in electrocatalysis: Insights into materials design. Science 2017, 355, 146-+.

(40) He, W.; Wang, Y.; Jiang, C.; Lu, L., Structural effects of a carbon matrix in non-precious metal O_2-reduction electrocatalysts. Chem. Soc. Rev 2016, 45, 2396-2409.

(41) Zou, L.; Hou, C. C.; Liu, Z.; Pang, H.; Xu, Q., Superlong Single-Crystal Metal-Organic Framework Nanotubes. J. Am. Chem. Soc 2018, 140, 15393-15401.

(42) Wu, Z. Y.; Xu, X. X.; Hu, B. C.; Liang, H. W.; Lin, Y.; Chen, L. F.; Yu, S. H., Iron Carbide Nanoparticles Encapsulated in Mesoporous Fe-N-Doped Carbon Nanofibers for Efficient Electrocatalysis. Angew. Chem 2015, 54, 8179-8183.

(43) Ma, R.; Zhou, Y.; Hu, C.; Yang, M.; Wang, F.; Yan, K.; Liu, Q.; Wang, J., Post iron-doping of activated nitrogen-doped carbon spheres as a high-activity oxygen reduction electrocatalyst. Energy Storage Mater 2018, 13, 142-150.

(44) Cheon, J. Y.; Kim, T.; Choi, Y.; Jeong, H. Y.; Kim, M. G.; Sa, Y. J.; Kim, J.; Lee, Z.; Yang, T.-H.; Kwon, K.; Terasaki, O.; Park, G.-G.; Adzic, R. R.; Joo, S. H., Ordered mesoporous porphyrinic carbons with very high electrocatalytic activity for the oxygen reduction reaction. Sci. Rep 2013, 3, 2715.

(45) Dombrovskis, J. K.; Jeong, H. Y.; Fossum, K.; Terasaki, O.; Palmqvist, A. E. C., Transition Metal Ion-Chelating Ordered Mesoporous Carbons as Noble Metal-Free Fuel Cell Catalysts. Chem. Mater 2013, 25, 856-861.

(46) Liang, H. W.; Wei, W.; Wu, Z. S.; Feng, X.; Mullen, K., Mesoporous metal-nitrogen-doped carbon electrocatalysts for highly efficient oxygen reduction reaction. J. Am. Chem. Soc 2013, 135, 16002-16005.

(47) Serov, A.; Artyushkova, K.; Atanassov, P., Fe-N-C Oxygen Reduction Fuel Cell Catalyst Derived from Carbendazim: Synthesis, Structure, and Reactivity. Adv. Energy Mater 2014, 4, 1301735.

(48) Niu, W.; Li, L.; Liu, X.; Wang, N.; Liu, J.; Zhou, W.; Tang, Z.; Chen, S., Mesoporous N-doped carbons prepared with thermally removable nanoparticle templates: an efficient electrocatalyst for oxygen reduction reaction. J. Am. Chem. Soc 2015, 137, 5555-5562.

(49) Qiao, Y.; Yuan, P.; Hu, Y.; Zhang, J.; Mu, S.; Zhou, J.; Li, H.; Xia, H.; He, J.; Xu, Q., Sulfuration of an Fe-N-C Catalyst Containing FexC/Fe Species to Enhance the Catalysis of Oxygen Reduction in Acidic Media and for Use in Flexible Zn-Air Batteries. Adv. Mater 2018, 30, 1804504.

(50) Wang, J. P.; Han, G. K.; Wang, L. G.; Du, L.; Chen, G. Y.; Gao, Y. Z.; Ma, Y. L.; Du, C. Y.; Cheng, X. Q.; Zuo, P. J.; Yin, G. P., ZIF-8 with Ferrocene Encapsulated: A Promising Precursor to Single-Atom Fe Embedded Nitrogen-Doped Carbon as Highly Efficient Catalyst for Oxygen Electroreduction. Small 2018, 14, 1704282.

(51) Fu, S. F.; Zhu, C. Z.; Su, D.; Song, J. H.; Yao, S. Y.; Feng, S.; Engelhard, M. H.; Du, D.; Lin, Y. H., Porous Carbon-Hosted Atomically Dispersed Iron-Nitrogen Moiety as Enhanced Electrocatalysts for Oxygen Reduction Reaction in a Wide Range of pH. Small 2018, 14, 1703118.

(52) Wang, Z.; Jin, H.; Meng, T.; Liao, K.; Meng, W.; Yang, J.; He, D.; Xiong, Y.; Mu, S., Fe, Cu-Coordinated ZIF-Derived Carbon Framework for Efficient Oxygen Reduction Reaction and Zinc-Air Batteries. Adv. Funct. Mater 2018, 28, 1802596.

(53) Jin, H.; Zhou, H.; He, D.; Wang, Z.; Wu, Q.; Liang, Q.; Liu, S.; Mu, S., MOF-derived 3D Fe-N-S co-doped carbon matrix/nanotube nanocomposites with advanced oxygen reduction activity and stability in both acidic and alkaline media. Appl Catal B: Environ 2019, 250, 143-149.

(54) Jin, H.; Zhou, H.; Li, W.; Wang, Z.; Yang, J.; Xiong, Y.; He, D.; Chen, L.; Mu, S., In situ derived Fe/N/S-codoped carbon nanotubes from ZIF-8 crystals as efficient electrocatalysts for the oxygen reduction reaction and zinc-air batteries. J. Mater. Chem. A 2018, 6, 20093-20099.

(55) Chung, D. Y.; Lee, K. J.; Yu, S. H.; Kim, M.; Lee, S. Y.; Kim, O. H.; Park, H. J.; Sung, Y. E., Alveoli-Inspired Facile Transport Structure of N-Doped Porous Carbon for Electrochemical Energy Applications. Adv. Energy Mater 2015, 5, 1401309.

(56) Ahn, S. H.; Yu, X.; Manthiram, A., "Wiring" Fe-Nx-Embedded Porous Carbon Framework onto 1D Nanotubes for Efficient Oxygen Reduction Reaction in Alkaline and Acidic Media. Adv. Mater 2017, 29, 1606534.

(57) Zhang, W.; Wu, Z. Y.; Jiang, H. L.; Yu, S. H., Nanowire-directed templating synthesis of metal-organic framework nanofibers and their derived porous doped carbon nanofibers for enhanced electrocatalysis. J. Am. Chem. Soc 2014, 136, 14385-14388.

(58) Liu, A.; Chen, X.; Zhang, Z.; Jiang, Y.; Shi, C., Selective synthesis and magnetic properties of FeSe2 and FeTe2 nanocrystallites obtained through a hydrothermal co-reduction route. Solid State Commun 2006, 138, 538-541.

(59) Wang, S.; Yu, D.; Dai, L., Polyelectrolyte Functionalized Carbon Nanotubes as Efficient Metal-free Electrocatalysts for Oxygen Reduction. J. Am. Chem. Soc 2011, 133, 5182-5185.

(60) Yang, Z. K.; Lin, L.; Xu, A.-W., 2D Nanoporous Fe-N/C Nanosheets as Highly Efficient Non-

Platinum Electrocatalysts for Oxygen Reduction Reaction in Zn-Air Battery. Small 2016, 12, 5710-5719.

(61) Hu, C.; Dai, L., Doping of Carbon Materials for Metal-Free Electrocatalysis. Adv. Mater 2019, 31, 1804672.

(62) Fu, X.; Zamani, P.; Choi, J.-Y.; Hassan, F. M.; Jiang, G.; Higgins, D. C.; Zhang, Y.; Hoque, M. A.; Chen, Z., In Situ Polymer Graphenization Ingrained with Nanoporosity in a Nitrogenous Electrocatalyst Boosting the Performance of Polymer-Electrolyte-Membrane Fuel Cells. Adv. Mater 2017, 29, 1604456.

(63) Park, K. S.; Ni, Z.; Cote, A. P.; Choi, J. Y.; Huang, R.; Uribe-Romo, F. J.; Chae, H. K.; O'Keeffe, M.; Yaghi, O. M., Exceptional chemical and thermal stability of zeolitic imidazolate frameworks. Proc. Natl. Acad. Sci. USA 2006, 103, 10186-10191.

(64) Bux, H.; Liang, F.; Li, Y.; Cravillon, J.; Wiebcke, M.; Caro, J., Zeolitic Imidazolate Framework Membrane with Molecular Sieving Properties by Microwave-Assisted Solvothermal Synthesis. J. Am. Chem. Soc 2009, 131, 16000-+.

(65) Haider, M. R.; Jiang, W.-L.; Han, J.-L.; Sharif, H. M. A.; Ding, Y.-C.; Cheng, H.-Y.; Wang, A.-J., In-situ electrode fabrication from polyaniline derived N-doped carbon nanofibers for metal-free electro-Fenton degradation of organic contaminants. Appl Catal B: Environ 2019, 256, 117774.

(66) Gao, R.; Dai, Q.; Du, F.; Yan, D.; Dai, L., C-60-Adsorbed Single-Walled Carbon Nanotubes as Metal-Free, pH-Universal, and Multifunctional Catalysts for Oxygen Reduction, Oxygen Evolution, and Hydrogen Evolution. J. Am. Chem. Soc 2019, 141, 11658-11666.

(67) Jiang, W.-J.; Gu, L.; Li, L.; Zhang, Y.; Zhang, X.; Zhang, L.-J.; Wang, J.-Q.; Hu, J.-S.; Wei, Z.;

Wan, L.-J., Understanding the High Activity of Fe-N-C Electrocatalysts in Oxygen Reduction: Fe/Fe$_3$C Nanoparticles Boost the Activity of Fe-N-x. J. Am. Chem. Soc 2016, 138, 3570-3578.

(68) Jiang, R.; Li, L.; Sheng, T.; Hu, G.; Chen, Y.; Wang, L., Edge-Site Engineering of Atomically Dispersed Fe-N4 by Selective C-N Bond Cleavage for Enhanced Oxygen Reduction Reaction Activities. J. Am. Chem. Soc 2018, 140, 11594-11598.

(69) Kim, S. J.; Mahmood, J.; Kim, C.; Han, G. F.; Kim, S. W.; Jung, S. M.; Zhu, G.; De Yoreo, J. J.; Kim, G.; Baek, J. B., Defect-Free Encapsulation of Fe(0) in 2D Fused Organic Networks as a Durable Oxygen Reduction Electrocatalyst. J. Am. Chem. Soc 2018, 140, 1737-1742.

(70) Liu, S. H.; Wang, Z. Y.; Zhou, S.; Yu, F. J.; Yu, M. Z.; Chiang, C. Y.; Zhou, W. Z.; Zhao, J. J.; Qiu, J. S., Metal-Organic-Framework-Derived Hybrid Carbon Nanocages as a Bifunctional Electrocatalyst for Oxygen Reduction and Evolution. Adv. Mater 2017, 29, 1700874.

(71) Kudin, K. N.; Ozbas, B.; Schniepp, H. C.; Prud'homme, R. K.; Aksay, I. A.; Car, R., Raman spectra of graphite oxide and functionalized graphene sheets. Nano Lett 2008, 8, 36-41.

(72) Zhang, G.; Lu, W.; Cao, F.; Xiao, Z.; Zheng, X., N-doped graphene coupled with Co nanoparticles as an efficient electrocatalyst for oxygen reduction in alkaline media. J. Power Source 2016, 302, 114-125.

(73) Pan, F. P.; Jin, J. T.; Fu, X. G.; Liu, Q.; Zhang, J. Y., Advanced Oxygen Reduction Electrocatalyst Based on Nitrogen-Doped Graphene Derived from Edible Sugar and Urea. ACS Appl. Mater. Interfaces 2013, 5, 11108-11114.

(74) Guo, D. H.; Shibuya, R.; Akiba, C.; Saji, S.; Kondo, T.; Nakamura, J., Active sites of nitrogen-doped carbon materials for oxygen reduction reaction clarified using model catalysts. Science 2016, 351, 361-365.

(75) Gong, K. P.; Du, F.; Xia, Z. H.; Durstock, M.; Dai, L. M., Nitrogen-Doped Carbon Nanotube Arrays with High Electrocatalytic Activity for Oxygen Reduction. Science 2009, 323, 760-764.

(76) Zhao, Z. H.; Li, M. T.; Zhang, L. P.; Dai, L. M.; Xia, Z. H., Design Principles for Heteroatom-Doped Carbon Nanomaterials as Highly Efficient Catalysts for Fuel Cells and Metal-Air Batteries. Adv. Mater 2015, 27, 6834-+.

(77) Geng, D.; Chen, Y.; Chen, Y.; Li, Y.; Li, R.; Sun, X.; Ye, S.; Knights, S., High oxygen-reduction activity and durability of nitrogen-doped graphene. Energy Environ Sci 2011, 4, 760-764.

(78) Liu, R. L.; Wu, D. Q.; Feng, X. L.; Mullen, K., Nitrogen-Doped Ordered Mesoporous Graphitic Arrays with High Electrocatalytic Activity for Oxygen Reduction. Angew. Chem, Int. Ed 2010, 49, 2565-2569.

(79) Zhou, D.; Yang, L. P.; Yu, L. H.; Kong, J. H.; Yao, X. Y.; Liu, W. S.; Xu, Z. C.; Lu, X. H., Fe/N/C hollow nanospheres by Fe(III)-dopamine complexation-assisted one-pot doping as nonprecious-metal electrocatalysts for oxygen reduction. Nanoscale 2015, 7, 1501-1509.

(80) Jiang, H. L.; Yao, Y. F.; Zhu, Y. H.; Liu, Y. Y.; Su, Y. H.; Yang, X. L.; Li, C. Z., Iron Carbide Nanoparticles Encapsulated in Mesoporous Fe-N-Doped Graphene-Like Carbon Hybrids as Efficient Bifunctional Oxygen Electrocatalysts. ACS Appl. Mater. Interfaces 2015, 7, 21511-21520.

(81) Cheon, J. Y.; Kim, K.; Sa, Y. J.; Sahgong, S. H.; Hong, Y.; Woo, J.; Yim, S.-D.; Jeong, H. Y.; Kim, Y.; Joo, S. H., Graphitic Nanoshell/Mesoporous Carbon Nanohybrids as Highly Efficient and Stable Bifunctional Oxygen Electrocatalysts for Rechargeable Aqueous Na-Air Batteries. Adv. Energy Mater 2016, 6, 1501794.

(82) Ahn, S. H.; Klein, M. J.; Manthiram, A., 1D Co- and N-Doped Hierarchically Porous Carbon Nanotubes Derived from Bimetallic Metal Organic Framework for Efficient Oxygen and Tri-iodide

Reduction Reactions. Adv. Energy Mater 2017, 7, 1601979.

(83) Wang, B.; Wang, X.; Zou, J.; Yan, Y.; Xie, S.; Hu, G.; Li, Y.; Dong, A., Simple-Cubic Carbon Frameworks with Atomically Dispersed Iron Dopants toward High-Efficiency Oxygen Reduction. Nano Lett 2017, 17, 2003-2009.

(84) Woo, J.; Sa, Y. J.; Kim, J. H.; Lee, H.-W.; Pak, C.; Joo, S. H., Impact of Textural Properties of Mesoporous Porphyrinic Carbon Electrocatalysts on Oxygen Reduction Reaction Activity. ChemElectroChem 2018, 5, 1928-1936.

(85) Xiao, M. L.; Zhu, J. B.; Feng, L. G.; Liu, C. P.; Xing, W., Meso/Macroporous Nitrogen-Doped Carbon Architectures with Iron Carbide Encapsulated in Graphitic Layers as an Efficient and Robust Catalyst for the Oxygen Reduction Reaction in Both Acidic and Alkaline Solutions. Adv. Mater 2015, 27, 2521-2527.

(86) Wei, J.; Liang, Y.; Hu, Y. X.; Kong, B. A.; Simon, G. P.; Zhang, J.; Jiang, S. P.; Wang, H. T., A Versatile Iron-Tannin-Framework Ink Coating Strategy to Fabricate Biomass-Derived Iron Carbide/Fe-N-Carbon Catalysts for Efficient Oxygen Reduction. Angew. Chem, Int. Ed 2016, 55, 1355-1359.

(87) Lin, G.; Ma, R.; Zhou, Y.; Liu, Q.; Hu, C.; Yang, M.; Wang, J., Iron-nitrogen dual-doped three-dimensional mesoporous carbons for high-activity electrocatalytic oxygen reduction. Applied Materials Today 2018, 13, 174-181.

(88) Wan, X.; Liu, X.; Li, Y.; Yu, R.; Zheng, L.; Yan, W.; Wang, H.; Xu, M.; Shui, J., Fe–N–C electrocatalyst with dense active sites and efficient mass transport for high-performance proton exchange membrane fuel cells. Nat. Catal 2019, 2, 259-268.

(89) Kramm, U. I.; Herrmann-Geppert, I.; Behrends, J.; Lips, K.; Fiechter, S.; Bogdanoff, P., On an

Easy Way To Prepare Metal-Nitrogen Doped Carbon with Exclusive Presence of MeN$_4$-type Sites Active for the ORR. J. Am. Chem. Soc 2016, 138, 635-640.

TOC
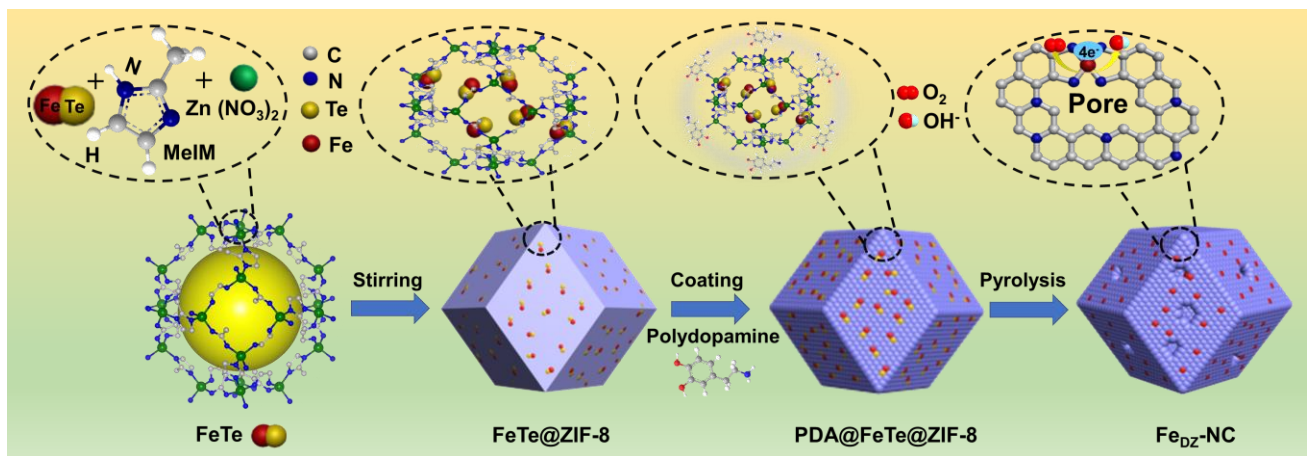
Synopsis: Fe-, N-embedded hierarchically porous carbon architectures derived from FeTe-trapped zeolitic imidazolate frameworks were demonstrated as efficient oxygen reduction electrocatalysts.